MAGNETOHYDRODYNAMICS Vol. 59 (2023), No. 3-4, pp. 365–377
DOI: 10.22364/mhd.59.3-4.9

MODELLING AZIMUTHAL VELOCITY OF LIQUID METAL IN A 2D CENTRIFUGAL SEPARATOR DRIVEN BY A TRAVELLING MAGNETIC FIELD

L. Terlizzi, R. Strazdiņš, L. Goldšteins

Institute of Physics, University of Latvia,
3 Jelgavas str., Riga LV-1004, Latvia

In this study we investigate the EM force and fluid velocity developed in a 2D liquid metal centrifugal system driven by a travelling magnetic field. A 2D axially symmetric numerical model has been developed using the COMSOL Multiphysics software, and distributions of pressure, azimuthal velocity and torque inside the centrifugal chamber were obtained. The average values for those distributions were successfully validated against a simple analytical model, showing that the presented numerical model can be used for a more in-depth analysis of the operating conditions of a centrifugal EM separator system. **Keywords**: centrifugal, electromagnetic, separator, velocity, numerical.

Introduction. Purification of liquid metal from small, unwanted solid particles that are by-products of industrial processes is a widespread problem in metallurgy. This is especially true for applications requiring high metal purity, such as the use of liquid metals as nuclear reactor coolants [1]. In practice, purification of the melt is achieved using common removal mechanisms such as sedimentation and filtration [2]. Another method is EM separation which uses electromagnetic fields to induce relative motion and separation of the impurities from the fluid due to their differing physical properties [2].

This paper investigates a centrifugal electromagnetic separator that uses the rotation of the fluid to induce centrifugal, separating forces on the impurities. Rotation of the liquid metal can be achieved with a travelling magnetic field. This field can be generated non-intrusively using externally rotating magnets, thus, the resulting system is completely contactless – no moving parts ever come into contact with the liquid metal. This improves both safety and separation efficiency [2] and is one of the reasons the EM separation technologies are being slowly introduced in the industry.

In this study the developed EM force density, azimuthal velocity, and pressure distribution in a 2D centrifugal system is investigated numerically and then compared to existing analytical descriptions. Information about distributions, especially for the azimuthal velocity, allows more precise modelling of forces acting on the impurities during the separation procedure.

1. System definition and analytical description.

Let us consider a cylindrical liquid metal chamber below which lies a disk with a permanent magnet system. The liquid metal chamber is completely sealed, and the external disk rotates while the chamber remains stationary. The rotation of the disk produces a travelling magnetic field within the chamber. It must be noted that the magnets lie below the outer rim of the chamber visible in Fig. 1, which shows the 2D simplification used to represent the described system. Thus, the external magnetic field in the outer rim area can be assumed to be in the form of a travelling wave using polar coordinates and complex numbers:

$$B_{\mathrm{e}}(\varphi, t) = B_0 \cdot \mathrm{e}^{i(m\varphi - \omega t)} \cdot \mathbf{e}_z, \tag{1}$$

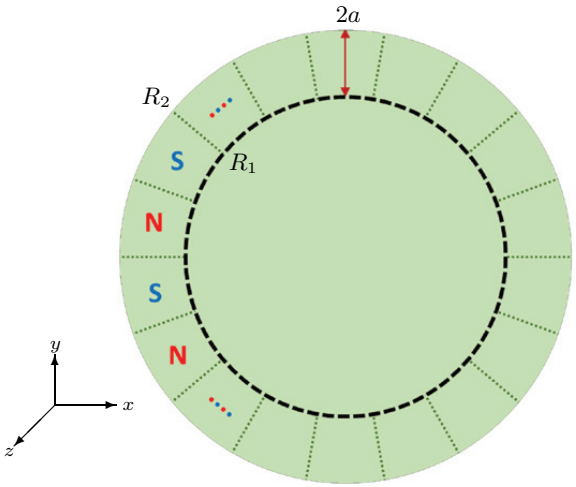

Fig. 1. Top view schematic of the centrifugal system. Magnets are placed below the outer rim in periodically opposite polarities. R_2 is the external radius of the chamber, R_1 is the radius at which external magnet placement begins.

Here B_0 is the constant characteristic magnetic field strength, m is the wave number of N-S pole pairs in the system, and ω is the angular frequency of the wave, defined as

$$\omega = 2\pi n m \tag{2}$$

where n is the rotational frequency of the external disk, or in other words the rpm of the motor.

From here on, a few important assumptions are made about the system. First, the height of the chamber is relatively small compared to the radius. Furthermore, the magnetic field strength is considered constant over the height, and so effects over the height are neglected.

Next, it is assumed that the fluid rotates as a solid body with a constant angular velocity, hence, the azimuthal velocity is proportional to the radius.

The curvature of the system is also neglected so that

$$R_2 - R_1 = \Delta R \ll R \tag{3}$$

It is also assumed that there is no radial flowrate, and furthermore it is assumed that processes happening outside the area enclosed by R_1 and R_2 do not meaningfully influence the dynamics of the system. This is referred to as the active area, and the expressions of the analytical description only pertain to the processes happening within it.

With these assumptions, it is possible to obtain an expression for the radially averaged azimuthal velocity in the outer rim area [3]:

$$v_\varphi = \frac{v_B N_\lambda}{2} \cdot \left(\sqrt{1 + \frac{4}{N_\lambda}} - 1 \right), \tag{4}$$

where N_λ is known as the interaction parameter, which is defined as

$$\mathrm{N}_\lambda = \frac{\sigma B_0^2 k_\mathrm{v} D_\mathrm{h}}{\lambda \rho v_B}, \tag{5}$$

where σ and ρ are the liquid metal conductivity and density, respectively; v_B is the mean tangential velocity of the magnet disk, D_h is the hydraulic diameter, and λ is a coefficient used to account for the friction in turbulent duct flows [3].

The factor k_v is the Voldek coefficient [4] which is used to consider the transversal end effect. This coefficient is a nonlinear function of the Rm_s and system geometry:

$$k_\mathrm{v} = \mathrm{Re}\left[\frac{\alpha^2}{\gamma^2}\left(1 - \frac{\tanh(\gamma a)}{\gamma a}\right)\right], \tag{6}$$

$$\gamma = \alpha\sqrt{1 - i\mathrm{Rm}_\mathrm{s}} \tag{7}$$

where α is the linear wave number and τ is half the wavelength:

$$\alpha = \frac{2\pi}{2\tau} \tag{8}$$

$$\tau = \frac{2\pi R}{2m} \tag{9}$$

The slip magnetic Reynolds number is defined as

$$\mathrm{Rm}_\mathrm{s} = \frac{\mu_0 \sigma (v_B - v_\varphi)}{\alpha}. \tag{10}$$

The azimuthal velocity of Eq. (4) can in turn be used to estimate the pressure developed over the radial direction [3]:

$$\Delta p = \frac{\rho}{2} \cdot \frac{R_2^2 - R_1^2}{R^2} \cdot v_\varphi^2 \tag{11}$$

where R is the mean radius between R_1 and R_2. From here, the radially averaged azimuthal EM force density on the system can be found [3]:

$$f_\varphi = \frac{\sigma B_0^2 k_\mathrm{v}}{2}(v_B - v_\varphi). \tag{12}$$

An estimate for the total system torque can be obtained by integrating the torque density $r f_\varphi \mathbf{e}_z$ over the active part of the chamber:

$$M = \int_0^b \mathrm{d}z \int_0^{2\pi} \mathrm{d}\varphi \int_{R_1}^{R_2} r f_\varphi \cdot r \mathrm{d}r = 2\pi b f_\varphi \cdot \frac{R_2^3 - R_1^3}{3}, \tag{13}$$

where b is the height of the chamber.

In order to use Eq. (4) and Eq. (11) to find the average azimuthal velocity and pressure over the radial profile, an iterative approach is used with an initial guess of $v_\varphi \approx \omega_B R/2$. Then the Voldek coefficient k_v, the friction factor λ and the interaction parameter N_λ are calculated to find a new v_φ according to Eq. (4). This cycle is repeated until v_φ has converged.

2. Numerical COMSOL model.

The numerical model is based on the same geometry as that of Fig. 1 and solved using the COMSOL Multiphysics commercial software. Coupled 2D Navier-Stokes and induction equations are solved with respect to the induced magnetic field amplitude using a time harmonic approach. In this model, the magnetic fields are defined as follows:

$$B_{\mathrm{e}} = B_{\mathrm{e}0}\,(x,y)\cdot \mathrm{e}^{i\omega t} \tag{14}$$

$$B_{\mathrm{i}} = B_{\mathrm{i}0}\,(x,y)\cdot \mathrm{e}^{i\omega t} \tag{15}$$

Here, no inherent assumption is made on the spatial distribution of the induced magnetic field, but the external magnetic field is known from Eq. (1). The $B_{\mathrm{i}0}$ is found from the following convection-diffusion equation:

$$i\omega\,(B_{\mathrm{e}0}+B_{\mathrm{i}0}) - v_x\frac{\partial B_{\mathrm{e}0}}{\partial x} - v_y\frac{\partial B_{\mathrm{e}0}}{\partial y} = -\frac{1}{\mu_0\sigma}\nabla^2 B_{\mathrm{i}0} + v_x\frac{\partial B_{\mathrm{i}0}}{\partial x} + v_y\frac{\partial B_{\mathrm{i}0}}{\partial y}. \tag{16}$$

This is done by the *cdeq* module. For Eq. (16) $B_{\mathrm{i}0}=0$ was used as a boundary condition on the walls of Fig. 2, corresponding to the non-conducting case, where the normal component of the induced current is zero at the boundary. The force density is then found from

$$\mathbf{j} = \left(\frac{1}{\mu_0}\cdot\frac{\partial B_{\mathrm{i}}}{\partial y}\right)\mathbf{e}_x - \left(\frac{1}{\mu_0}\cdot\frac{\partial B_{\mathrm{i}}}{\partial x}\right)\mathbf{e}_y, \tag{17}$$

$$\mathbf{f}_{\mathrm{em}} = \left(\frac{\Re\mathrm{e}\,[j_y\cdot B^*]}{2}\right)\mathbf{e}_x - \left(\frac{\Re\mathrm{e}\,[j_x\cdot B^*]}{2}\right)\mathbf{e}_y. \tag{18}$$

$$B = B_{\mathrm{e}} + B_{\mathrm{i}} \tag{19}$$

From the EM force of Eq. (18) an azimuthal semi-empirical friction force is added. This is given by the following equation [3]:

$$\mathbf{f}_{\mathrm{loss}} = -\frac{\lambda}{D_{\mathrm{h}}}\cdot\frac{\rho|\mathbf{v}|}{2}\,(v_x\mathbf{e}_x + v_y\mathbf{e}_y)\,. \tag{20}$$

The friction factor λ of Eq. (20) is updated in real time based on the current average azimuthal velocity of the simulation. The obtained volume force is then applied to the liquid metal to cause motion of the fluid. This is done by the *spf* module, which solves the following momentum equations:

$$\rho\,(\mathbf{v}\cdot\boldsymbol{\nabla})\,\mathbf{v} = -\boldsymbol{\nabla}p + \mathbf{f}_{\mathrm{em}} + \mathbf{f}_{\mathrm{loss}} + \mu\boldsymbol{\nabla}^2\mathbf{v}, \tag{21}$$

$$\boldsymbol{\nabla}\mathbf{v} = 0. \tag{22}$$

Liquid sodium at 140°C was used as a reference metal. The main material properties used in the simulation are listed in Table 1. The MUMPS solver was applied to solve the fully coupled problem, using the constant Newton method with a 0.2 damping factor. A triangular mesh with around 20000 elements was used (see Fig. 2), which also depicts the respective boundary conditions on the walls of the chamber. The mesh elements had an average area of $3.34\,\mathrm{mm}^2$ per element.

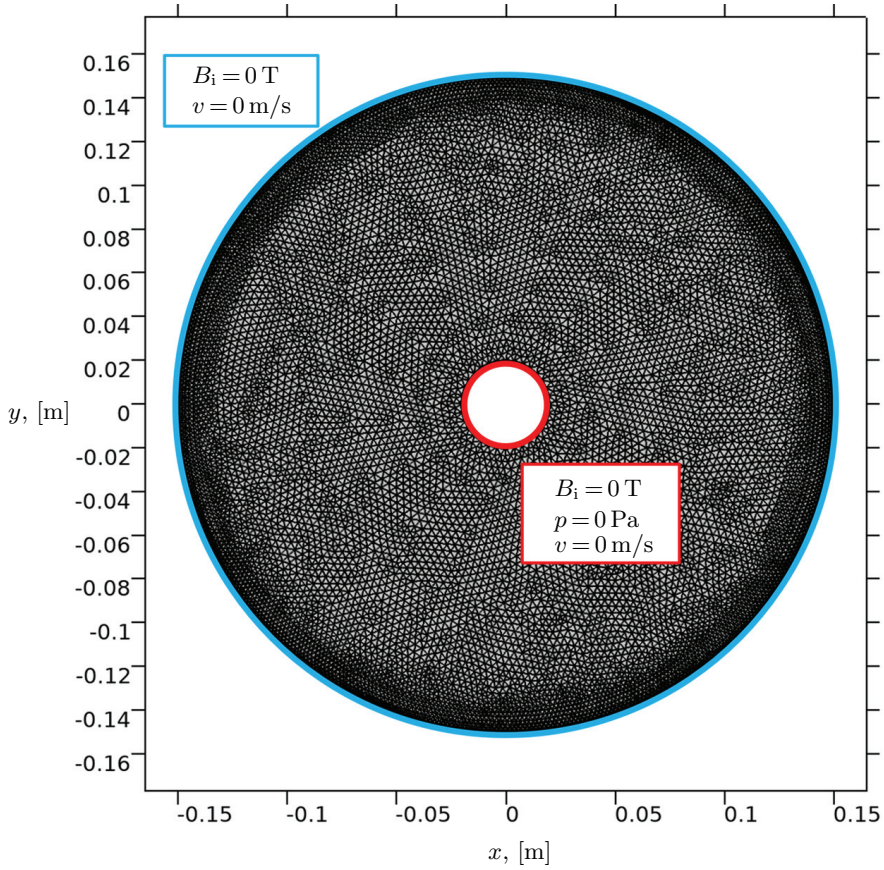

Fig. 2. Triangular COMSOL mesh used in the simulation. The text boxes show the respective boundary conditions.

3. Results.

For the case where the disk rotation rate was 1100 rpm, the external magnetic field acting on the system during the simulation is shown in Fig. 3, whereas the magnetic field that it induces is shown in Fig. 4. The place where the external magnetic field drops to zero, is the active area boundary R_1, which is usually accompanied by a sharp change in the dynamics of the system, such as in the liquid velocity in Fig. 5.

Fig. 6 depicts the full radial profile of relative velocity as the ratio of the liquid azimuthal velocity to the external magnet azimuthal velocity. Fig. 6 specifically shows that the solid body approximation becomes less valid as the rpm of the system increases. A more apt indicator for the validity of the solid body assumption is the interaction parameter N_λ. It has been shown [3] and analyzed [5] that for large N_λ values $v_\varphi \approx v_B$,

Table 1. Main system parameters.

σ, [S/m]	$9{\cdot}10^6$
ρ, [kg/m^3]	920
μ, [Pa·s]	$5.94{\cdot}10^{-4}$
B_0, [T]	0.20

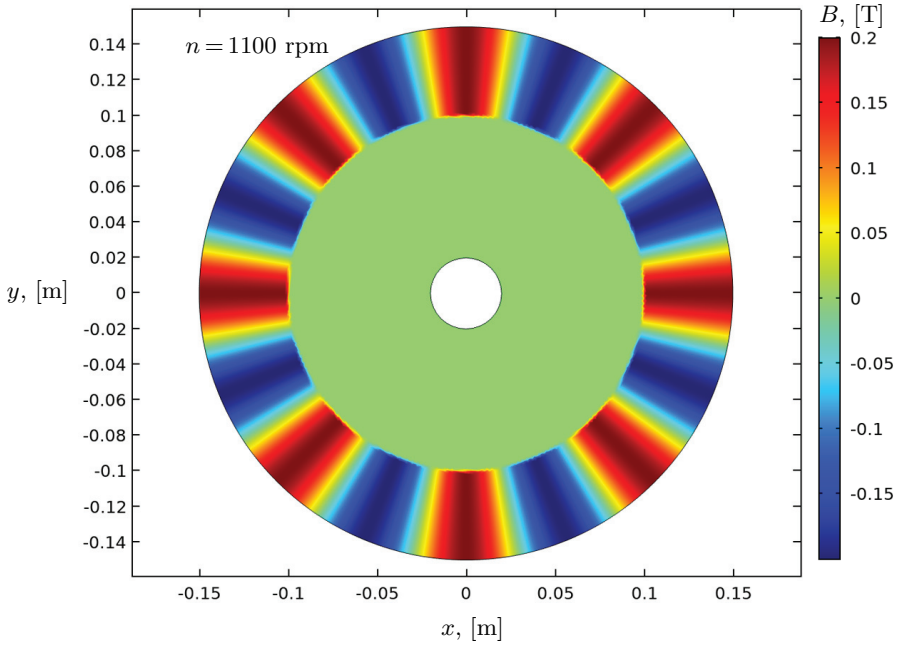

Fig. 3. External magnetic field.

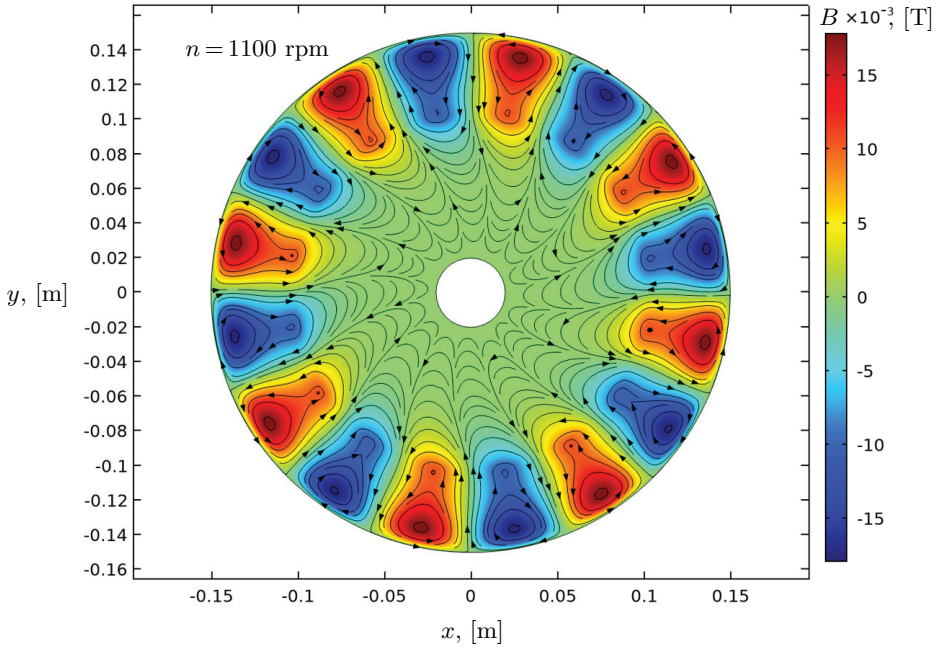

Fig. 4. Induced magnetic field and current density contour lines.

whereas for low N_λ values $v_\varphi \approx v_B\sqrt{N_\lambda}$. The higher this parameter the more the relative velocity profile of the fluid resembles that of solid body rotation, which in the absolute case is a horizontal line. Because N_λ is inversely proportional to the magnet speed as

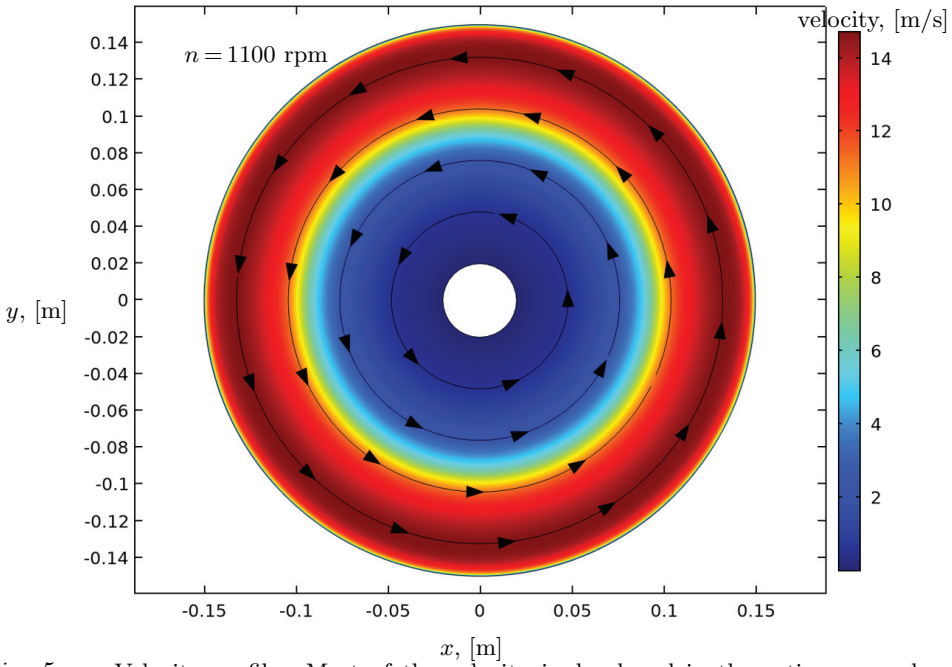

Fig. 5. Velocity profile. Most of the velocity is developed in the active area where the magnetic field is present.

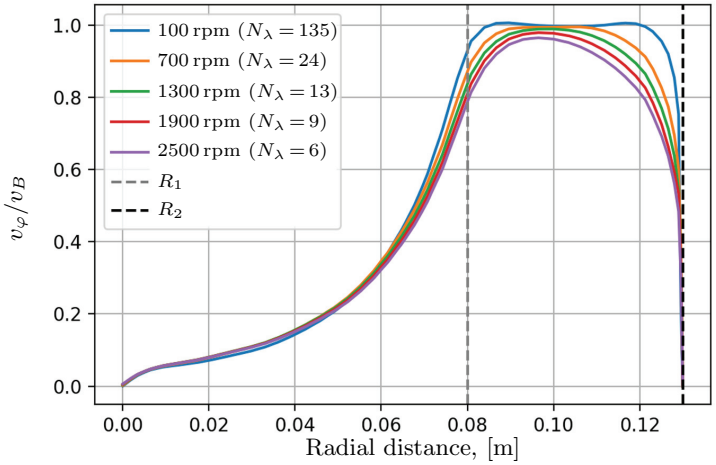

Fig. 6. Relative velocity profiles over the radial direction. The curves are the ratio between the fluid tangential velocity at a certain radial distance and the tangential velocity of the magnet disk at that same radial distance.

shown in Eq. (5), in this figure it is highest for the 100-rpm regime, which in fact is horizontal for almost the entire active area.

Fig. 7 shows the average system azimuthal velocity. This is the azimuthal velocity component averaged over the active radial profile. A comparison is shown between the

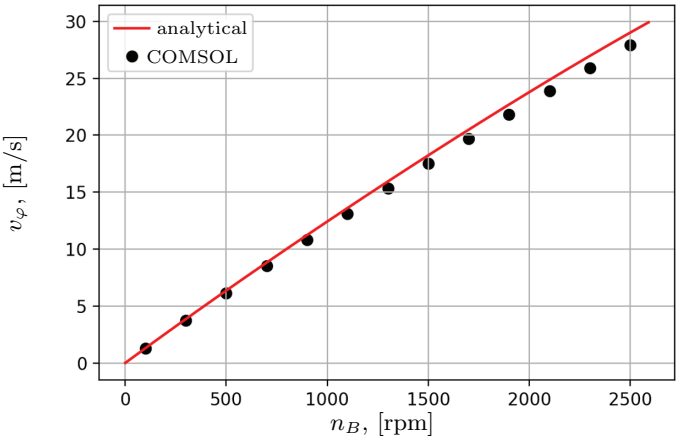

Fig. 7. Radially averaged azimuthal velocity in the active area as a function of the disk rpm (n_B).

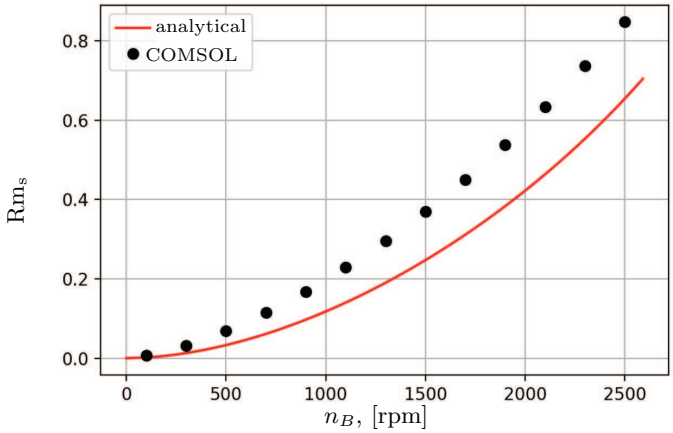

Fig. 8. Slip magnetic Reynolds number ($\mathrm{Rm_s}$) as a function of the disk rpm (n_B).

data points obtained with COMSOL and the method outlined in Eq. (4). The $\mathrm{Rm_s}$ is visible in Fig. 8, which shows that, as the rpm increases, the slip of the system does so too, along with $\mathrm{Rm_s}$.

Fig. 9 and Fig. 10 show the numerical pressure field and the radial profile in the chamber. The pressure in Fig. 11 is the pressure developed inside the active area only, meaning that for every disk rotation rate the pressure at the distance R_1 is subtracted from the pressure at the distance R_2 and plotted on this graph as a point. This is done because the analytical curve to which the numerical results are compared ignores the effects outside the active area. This analytical curve is calculated according to Eq. (11).

The ratio of the pressures at R_1 and R_2 is presented in Fig. 12, which clearly shows that the pressure at the active area boundary is around 13% of the total developed pressure. This deviation acts as an estimate to validate whether the processes happening outside the active area truly have an insignificant impact on the dynamics of the system, as it was assumed by the analytical model of [3].

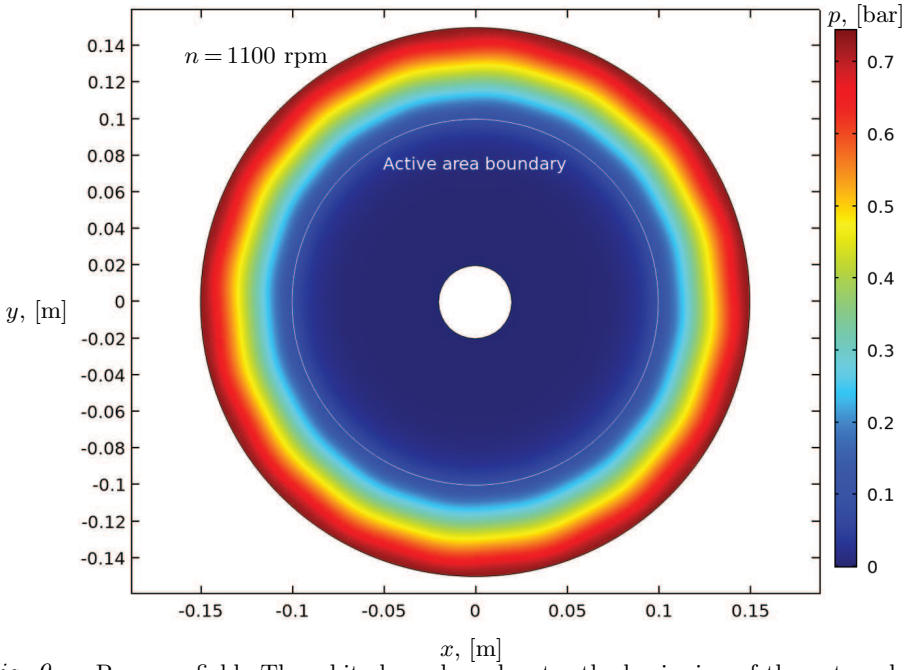

Fig. 9. Pressure field. The white boundary denotes the beginning of the external magnetic field.

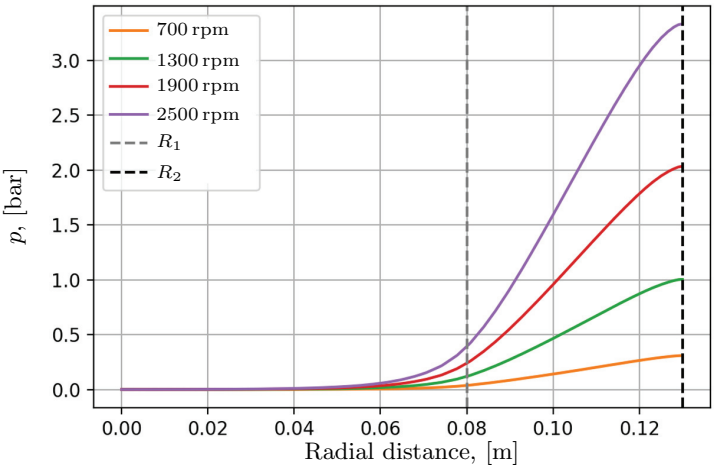

Fig. 10. Pressure profile over the radial direction.

The magnitude field for the azimuthal component of the EM force density is shown in Fig. 13, and the active radial profile for it is displayed in Fig. 14. Below the distance R_1 the EM force is simply zero because the external magnetic field is zero, hence, in this figure only the active radial portion is drawn. Because the distribution of the EM force density is not axially symmetric, unlike that of pressure and azimuthal velocity, the EM force density was averaged over every circumference of the radius r before drawing the radial profile of Fig. 14.

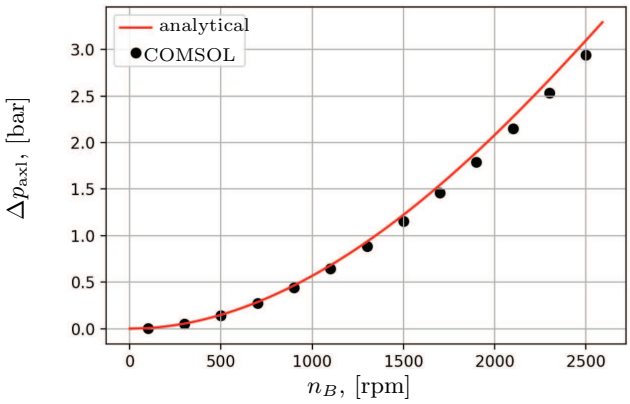

Fig. 11. Pressure difference developed over over the active area as a function of disk rpm (n_B).

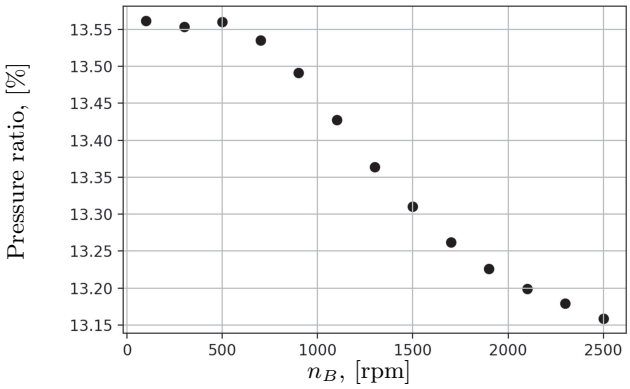

Fig. 12. Ratio of pressures at radius R_1 and R_2, in percentages, as a function of disk rpm (n_B).

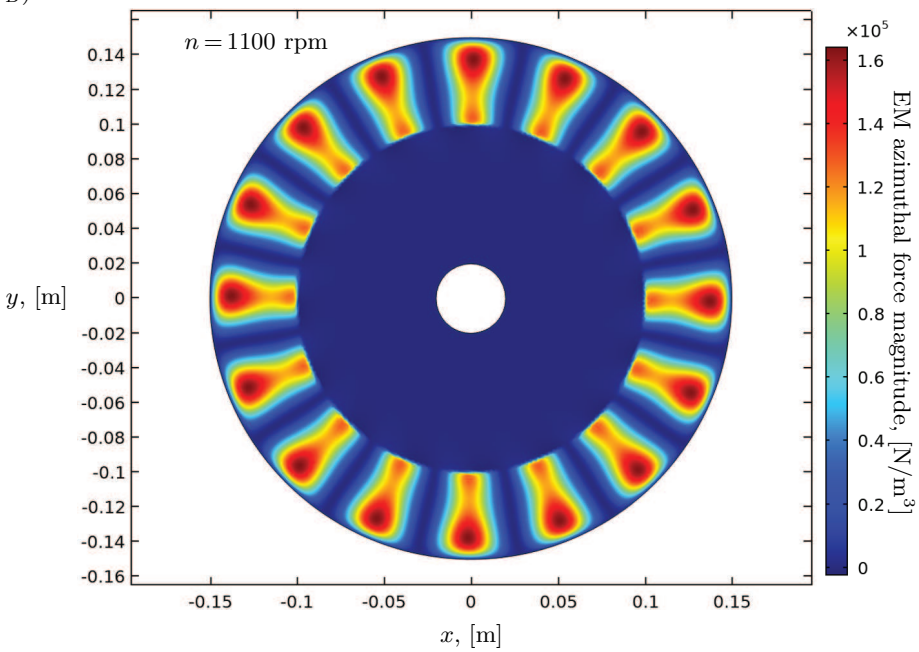

Fig. 13. Magnitude of the azimuthal EM force density component.

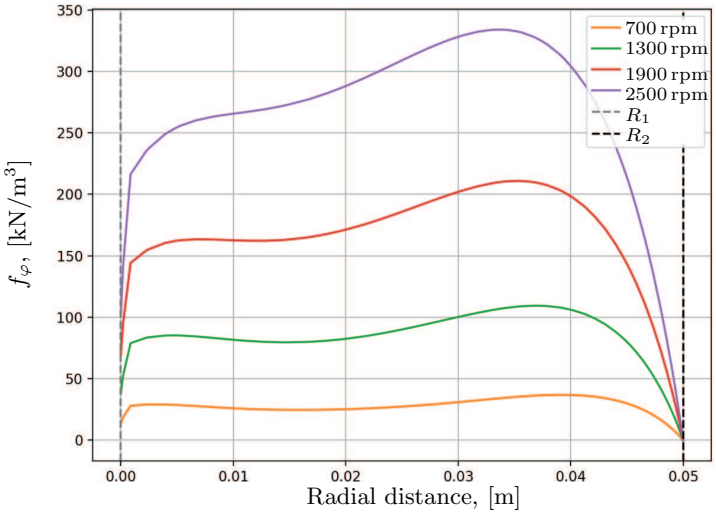

Fig. 14. Radial profile of the circumference-averaged azimuthal EM force density component.

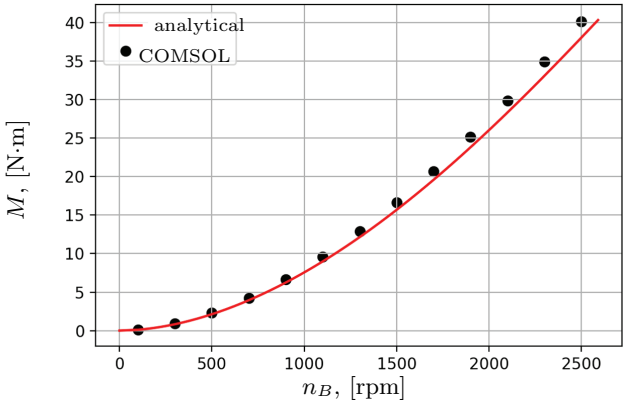

Fig. 15. Total system torque.

By calculating the average value for the profiles in Fig. 14 for every disk rotation rate, an estimation of the average azimuthal EM force density acting on the active domain can be obtained. This can be used instead of the analytical estimation of Eq. (12) to calculate the torque of Eq. (13). That is done to obtain the torque comparison in Fig. 15.

The presented comparisons of Fig. 7, Fig. 11, and Fig. 15 show an acceptable agreement between the numerical and analytical models. Fig. 16 shows the relative deviations of the analytical model from the numerical model for these figures. This relative deviation tends to stay below 10% for all 3 indicators.

4. Conclusions.

From the presented study it can be concluded that an acceptable agreement between the numerical and analytical models was achieved. Fig. 6 shows the validity of the solid fluid body rotation assumption for the calculation of the average azimuthal velocity in Eq. (4). As the magnet disk rpm increases, the interaction parameter N_λ decreases. This

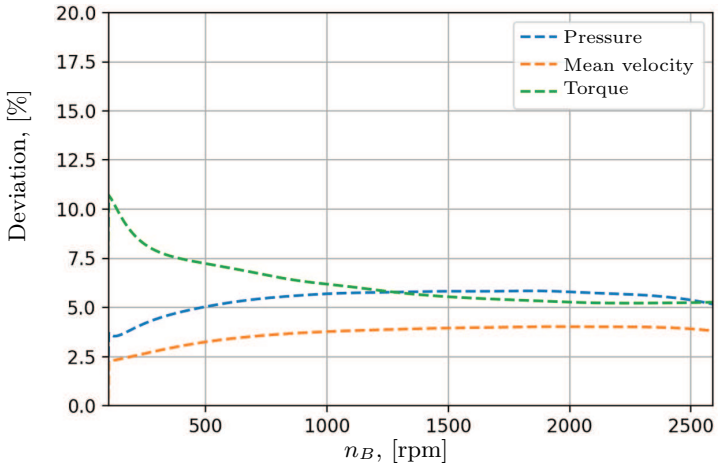

Fig. 16. Relative deviations from the numerical model as a function of the disk rpm (n_B).

is correlated with a change of the relative velocity profile, where the profile becomes less of a horizontal line, which is the solid body case, and begins to curve more.

Fig. 12 shows that in the profiles of Fig. 10 the pressure developed at the beginning of the active area is indeed only a small part of the total pressure developed by the system, as was assumed by the analytical description used to validate the numerical model.

It was also shown in Fig. 15 that the integral torque calculation of Eq. (13) can be used as a simple method to estimate the total torque produced by the centrifugal system.

Overall, the average values for the distributions produced by the numerical model match those of the analytical model of [3], which was successfully validated against experimental data. However, for the calculation of important EM filtration parameters, working only with average values can be rather limiting. Hence, the numerical model presented here offers a simple, first reference approximation that could be used for the prediction and validation of important EM filtration parameters in separators and similar systems.

One important point is that, in practice, most of the friction present in the system arises from the effects over the height of the chamber, which is considerably smaller than the radial dimension. In the studied 2D model, the semi-empirical friction force of Eq. (20) was used to capture this behavior over the third dimension. However, that is a rather simple assumption.

For a more complete representation of turbulence effects (friction force) over the height, a 3D simulation with turbulence models like RANS, for instance, should be used instead. This kind of approach would remove the need for a semi-empirical friction force term and would also be able to describe additional phenomena that the 2D model is simply unable to capture, such as vortices in the meridional plane that could affect the separator efficiency. That is why work towards such a model is planned in future studies.

References

[1] K.K. Rajan. A study on sodium-the fast breeder reactor coolant. In: *IOP Conference Series: Materials Science and Engineering. IOP Publishing*, vol. 1045 (2021), no. 1, p. 012013.

[2] L. Zhang, S. Wang, A. Dong, J. Gao and L. Damoah. Application of electromagnetic (EM) separation technology to metal refining processes: a review. *Metallurgical and Materials Transactions B*, vol. 45 (2014), pp. 2153–2185.

[3] L. Goldsteins, I. Bucenieks, L. Buligins. A simplified model of the centrifugal electromagnetic induction pump (CEMIP) with rotating permanent magnets. *Magnetohydrodynamics*, vol. 50 (2014), no. 2, pp. 165–178.

[4] A.I. Voldek. *Induction Magnetohydrodynamic Machines with a Liquid Metal Working Body* (Energia Publ. House, Leningrad, 1974) (in Russ.).

[5] L. Goldšteins. Numerical study of a centrifugal electromagnetic induction pump with zero flowrate. *Magnetohydrodynamics*, vol. 58 (2022), no. 1–2, pp. 167–176.

Received 16.12.2023